INTERNATIONAL JOURNAL FOR NUMERICAL METHODS IN FLUIDS
Int. J. Numer. Meth. Fluids 2005; **49**:603–618
Published online 3 August 2005 in Wiley InterScience (www.interscience.wiley.com). DOI: 10.1002/fld.1017

Fourth- and tenth-order compact finite difference solutions of perturbed circular vortex flows

P. J. S. A. Ferreira de Sousa*,† and J. C. F. Pereira‡

Department of Mechanical Engineering/LASEF, Instituto Superior Técnico (IST), Av. Rovisco Pais, 1, 1049-001 Lisbon, Portugal

SUMMARY

In this study, high-order compact finite difference calculations are reported for 2D unsteady incompressible circular vortex flow in primitive variable formulation. The fourth-order Runge–Kutta temporal discretization is used together with fourth- or tenth-order compact spatial discretization. Dependent on the perturbation initially imposed, the solutions display a tripole, triangular or square vortex. The comparison of the predictions with the detailed spectral calculations of Kloosterziel and Carnevale (*J. Fluid Mech.* 1999; **388**:217–257) shows that the vorticity fields are very well captured. The spectral resolution of the present method was quantified from the decomposition of the vorticity distribution in its azimuthal components and compared with reported spectral results. Using identical grid resolution to the reference results yields negligible differences in the main features of the flow. The perturbation amplitude and its first harmonic are virtually identical to the reference results for both fourth- or tenth-order spatial discretization, as theoretically expected but seldom *a posteriori* verified. The differences between the two spatial discretizations appear only for coarser grids, favouring the tenth-order discretization.

KEY WORDS: high-order; compact finite differences; incompressible Navier–Stokes; circular vortex

1. INTRODUCTION

High-order accuracy of the numerical simulation of unsteady incompressible fluid flow is required for turbulent flow research through direct numerical simulation (DNS) or large-eddy simulation (LES), but also for complex engineering applications in order to decrease the number of nodes of the discrete domain. High-order compact finite differences have spectral-like

*Correspondence to: P. J. S. A. Ferreira de Sousa, Department of Mechanical Engineering/LASEF, Instituto Superior Técnico (IST), Av. Rovisco Pais, 1, 1049-001 Lisbon, Portugal.
†E-mail: psousa@navier.ist.utl.pt
‡E-mail: jose@navier.ist.utl.pt

Contract/grant sponsor: FCT; contract/grant number: SFRH/BD/1129/2000

Received 24 December 2004
Revised 3 May 2005
Accepted 4 May 2005

resolution in the sense of low dissipation and dispersion with narrow stencils, see Reference [1], and are a logical choice if one is looking for high accuracy and flexibility at a relatively low cost.

For incompressible flows, the applications that use compact finite difference schemes in primitive variables either do not use compact schemes in the Poisson pressure equation [2, 3], or use artificial compressibility [4] in order to avoid the solution of an elliptical multi-dimensional equation with compact operators. Many applications using high-order finite difference schemes for the spatial discretization use lower-order schemes for explicit time advancement, e.g. Reference [5], resulting in methods that have high order only for the spatial discretization and thus have very restrictive stability limits. Some DNS applications combine spectral derivatives in two homogeneous coordinate directions with eighth order [6] or up to tenth order, e.g. Reference [7], compact schemes for the remaining non-homogenous direction. Using eighth/tenth-order compact schemes as those proposed by Lele [1] requires solving penta-diagonal matrices, as opposed to fourth/sixth-order compact schemes that solve tri-diagonal matrices, meaning that the increase formal accuracy carries a substantial computational cost. However, very few studies investigate the *a posteriori* error induced by spatial and temporal discretizations of different orders of accuracy.

The main objective of this work is to calculate a demanding circular vortex flow using up to tenth-order spatial discretization and a consistent Poisson discretization, and compare with reported spectral solutions. This is done in the framework of 2D unsteady incompressible flow in primitive variable formulation, solved with a projection method and fourth-order Runge–Kutta temporal discretization. This numerical framework was chosen since it resorts to well-proven and increasingly popular numerical techniques in order to achieve high-order accuracy. With such a solver in hand, and through comparison with spectral results, it is possible to investigate the performance of fourth- and tenth-order accurate spatial discretizations in a strongly non-linear flow governed by the full 2D Navier–Stokes equations. The test problem used for the comparison is a dynamically rich flow, that through the development of its wave-related instabilities provides a number of tests for the numerical method employed.

The instability of 2D isolated circular vortices presents itself as a good benchmark to test numerical schemes. Monopolar vortices may emerge in two-dimensional turbulence from an initial state of randomly distributed vorticity, see Reference [8]. When two of such vortices with oppositely signed circulations meet, a dipole can form. A dipole is a self-propelling compound vortex. In forced two-dimensional turbulence, Legras *et al.* [9] observed a more complex coherent compound vortex, the tripole, which is characterized by an elliptic vortex surrounded by two satellite vortices rotating in the opposite direction. The formation of tripoles from unstable monopolar vortices was first predicted by Leith [10]. Later on, this transition was verified in experiments with rotating fluids [11, 12], as well as in numerical work [13]. The cited laboratory experiments [11] and numerical simulations [13] showed that tripole formation is the result of an azimuthal wavenumber-2 instability of an unstable isolated circular vortex. A tripolar structure, consisting of an anti-cyclonic core and two cyclonic satellites, with a period of rotation of 18 days and characteristic dimensions of about 50–70 km, was visible in the sea of the Bay of Biscay during the period May 1991–February 1992, Reference [14] in Reference [15]. Through further laboratory experiments, Kloosterziel and van Heijst [16] showed that wavenumber-3 instabilities lead to a triangular vortex, surrounded by three smaller vortices. The tripole and triangular vortex have simple symmetric vorticity distributions. A wavenumber-4 instability leads to a square vortex, which is surrounded by

four smaller vortices. The square vortex, unlike the tripole and the triangular vortex, is unstable and breaks up into two dipoles. The high-order compact finite difference solutions of the unsteady incompressible Navier–Stokes for the three different perturbations will be compared with the spectral results of Reference [15].

In the next section of this paper, we present the numerical model employed to solve the two-dimensional unsteady incompressible Navier–Stokes equations. The spatial discretization uses a staggered grid and the derivatives are evaluated using fourth- or tenth-order compact finite difference schemes. The time advancement is performed with a fourth-order time accurate Runge–Kutta procedure. The compact finite difference Poisson equation for the pressure correction is solved with an alternate direction implicit (ADI) procedure. This is one of the main features of the method because the accuracy of the method is preserved for both velocities and pressure. This is followed by the presentation of the results grouped into two subsections. Firstly, the accuracy of the numerical method used is verified with analytical Navier–Stokes solutions. Secondly, the results for the calculations of three azimuthal perturbations to circular vortices and its comparison with spectral results are presented and discussed.

2. NUMERICAL METHOD

2.1. Navier–Stokes equations

The unsteady incompressible form of the continuity and Navier–Stokes equations for a Newtonian fluid were considered

$$\nabla \cdot \mathbf{u} = 0 \tag{1}$$

$$\frac{\partial \mathbf{u}}{\partial t} + (\mathbf{u} \cdot \nabla)\mathbf{u} = \nu \nabla^2 \mathbf{u} - \nabla p \tag{2}$$

where $\mathbf{u}$ is the fluid velocity, p the pressure (divided by density) and ν the kinematic viscosity of the fluid.

The momentum equations are spatially discretized on a staggered mesh by finite differences and all derivatives are evaluated with implicit fourth- or tenth-order compact finite difference schemes [1]. For the sake of simplicity, let us consider a uniformly spaced mesh where the nodes are indexed by i. The independent variable at the nodes is $x_i = h(i-1)$ for $1 \leqslant i \leqslant N$ and the function values at the nodes $f_i = f(x_i)$ are given. The finite difference approximation f'_i to the first derivative at the node i depends on the function values at nodes near i. These schemes are generalizations of the Padé scheme. These generalizations are derived by writing approximations of the form

$$\beta f'_{i-2} + \alpha f'_{i-1} + f'_i + \alpha f'_{i+1} + \beta f'_{i+2} = a\,\frac{f_{i+1} - f_{i-1}}{2h} + b\,\frac{f_{i+2} - f_{i-2}}{4h} + c\,\frac{f_{i+3} - f_{i-3}}{6h} \tag{3}$$

The relations between the coefficients α, β, a, b and c are derived by matching the Taylor series coefficients of various orders.

For the fourth-order tri-diagonal scheme (Classical Padé scheme):

$$\alpha = \tfrac{1}{4}, \quad \beta = 0, \quad a = \tfrac{3}{2}, \quad b = 0, \quad c = 0$$

For the tenth-order penta-diagonal scheme:

$$\alpha = \tfrac{1}{10}, \quad \beta = \tfrac{1}{20}, \quad a = \tfrac{17}{12}, \quad b = \tfrac{101}{150}, \quad c = \tfrac{1}{100}$$

The derivation of compact approximations for the second derivative is similar to the first derivative. Again we start with a relation of the following form:

$$\beta f''_{i-2} + \alpha f''_{i-1} + f''_i + \alpha f''_{i+1} + \beta f''_{i+2} = a\,\frac{f_{i+1} - 2f_i + f_{i-1}}{h^2} + b\,\frac{f_{i+2} - 2f_i + f_{i-2}}{4h^2} + c\,\frac{f_{i+3} - 2f_i + f_{i-3}}{9h^2} \tag{4}$$

where f''_i represents the finite difference approximation to the second derivative at node i. Once again, the relations between the coefficients α, β, a, b and c are derived by matching the Taylor series coefficients of various orders.

For the fourth-order tri-diagonal scheme:

$$\alpha = \tfrac{1}{10}, \quad \beta = 0, \quad a = \tfrac{6}{5}, \quad b = 0, \quad c = 0$$

For the tenth-order penta-diagonal scheme:

$$\alpha = \tfrac{334}{899}, \quad \beta = \tfrac{43}{1798}, \quad a = \tfrac{1065}{1798}, \quad b = \tfrac{1038}{899}, \quad c = \tfrac{79}{1798}$$

Formulas for calculating the first derivative on a cell-centred mesh are necessary in staggered grids. Starting from an approximation of the form

$$\beta f'_{i-2} + \alpha f'_{i-1} + f'_i + \alpha f'_{i+1} + \beta f'_{i+2} = a\,\frac{f_{i+1/2} - f_{i-1/2}}{h} + b\,\frac{f_{i+3/2} - f_{i-3/2}}{3h} + c\,\frac{f_{i+5/2} - f_{i-5/2}}{5h} \tag{5}$$

The relations between the coefficients α, β, a, b and c are derived yet again by matching the Taylor series coefficients of various orders.

For the fourth-order tri-diagonal scheme:

$$\alpha = \tfrac{1}{22}, \quad \beta = 0, \quad a = \tfrac{12}{11}, \quad b = 0, \quad c = 0$$

For the tenth-order penta-diagonal scheme:

$$\alpha = \tfrac{96850}{288529}, \quad \beta = \tfrac{9675}{577058}, \quad a = \tfrac{683425}{865587}, \quad b = \tfrac{505175}{577058}, \quad c = \tfrac{69049}{1731174}$$

The fourth-order accurate Runge–Kutta scheme was used for temporal discretization. Periodic boundary conditions were applied to all discrete operators used. In order to achieve fast convergence and low numerical noise, the periodic boundary conditions were implemented implicitly when solving the compact finite differences operators. This means that for every derivative being calculated, the matrices are factored using LU decomposition, so that when each derivative is calculated, only back substitutions are performed. This procedure allows for equal levels of numerical noise between the fourth- and tenth-order solutions, thus allowing a better comparison of the characteristics of both schemes.

2.2. Pressure correction equation

The numerical method used belongs to the projection methods class, which are based on the Helmholtz–Hodge decomposition theorem, see for example Reference [17]. This theorem states that any vector field $\mathbf{w}$ can be decomposed as

$$\mathbf{w} = \mathbf{u} + \nabla q \tag{6}$$

where $\mathbf{u}$ is divergence free and q is a scalar field defined implicitly as

$$\nabla \cdot \mathbf{w} = \nabla^2 q \tag{7}$$

We can define an operator P that projects a vector field onto its divergence-free part:

$$\mathbf{u} = P\mathbf{w} = \mathbf{w} - \nabla q \tag{8}$$

The left-hand side of the Navier–Stokes equation for incompressible flow written as

$$\frac{\partial \mathbf{u}}{\partial t} + \nabla p = -(\mathbf{u} \cdot \nabla)\mathbf{u} + v\nabla^2 \mathbf{u} \tag{9}$$

is a Helmholtz–Hodge decomposition. Therefore an equivalent projection formula is given by

$$\frac{\partial \mathbf{u}}{\partial t} + \nabla p = P[-(\mathbf{u} \cdot \nabla)\mathbf{u} + v\nabla^2 \mathbf{u}] \tag{10}$$

where P is the operator which projects a vector field onto the space of divergence-free vector fields with appropriate boundary conditions.

The classical four-stage fourth-order Runge–Kutta temporal discretization scheme is used with periodic boundary conditions in every stage to advance the equations from time n to $n+1$. Starting with $\mathbf{u}^n$ we compute

$$\begin{aligned} \mathbf{u}^{n+1} &= \mathbf{u}^n + \frac{\Delta t}{6}(k_1 + 2k_2 + 2k_3 + k_4) - \Delta t G p^{n+1} \\ M\mathbf{u}^{n+1} &= 0 \end{aligned} \tag{11}$$

where

$$k_i = (-C + D)(\mathbf{u}_i), \quad i = 1, \ldots, 4 \tag{12}$$

and

$$\mathbf{u}_1 = \mathbf{u}^n \tag{13}$$

$$\begin{aligned} \mathbf{u}_2 &= \mathbf{u}^n + \frac{\Delta t}{2}(-C + D)(\mathbf{u}_1) - \frac{\Delta t}{2} G p_2 \\ M\mathbf{u}_2 &= 0 \end{aligned} \tag{14}$$

$$\begin{aligned} \mathbf{u}_3 &= \mathbf{u}^n + \frac{\Delta t}{2}(-C + D)(\mathbf{u}_2) - \frac{\Delta t}{2} G p_3 \\ M\mathbf{u}_3 &= 0 \end{aligned} \tag{15}$$

$$\begin{aligned} \mathbf{u}_4 &= \mathbf{u}^n + \Delta t(-C+D)(\mathbf{u}_3) - \Delta t G p_4 \\ M\mathbf{u}_4 &= 0 \end{aligned} \tag{16}$$

where M is the discrete divergence operator, G the discrete gradient operator and C, D represent convective and diffusive operators, respectively. In order to solve $(\mathbf{u}_i, p_i)$ for stages $i = 2, 3, 4, n+1$, first an intermediate velocity $\mathbf{u}_i^*$ is obtained. Then this quantity is projected onto the space of divergence-free fields to yield $\mathbf{u}_i$. For each stage, and denoting by $\phi_i = p_i - p_{i-1}$ the pressure correction, this procedure is given by

Step 1: Solve for the intermediate field u_i^*.
Step 2: Perform the projection.

$$\mathbf{u}_i = \mathbf{u}_i^* + \Delta t G\phi \tag{17}$$

$$M(\mathbf{u}_i) = 0 \tag{18}$$

$$M(G\phi_i) = -\frac{1}{\Delta t} M(\mathbf{u}_i^*) \tag{19}$$

Step 3: Update the velocity and pressure.

2.3. 2D Poisson solver

The discretization of (19) using compact operators requires a formidable computing time to solve the full matrix. Therefore, the Poisson equation was modified in order to use an ADI procedure. In order to solve Equation (19), a pseudo-temporal term $\partial\phi/\partial\tau$ is added to this equation and the resulting equation is solved by an ADI iterative procedure that uses compact finite difference schemes. The pseudo-temporal term vanishes in the convergence of the ADI iterative procedure

$$\left.\frac{\partial\phi}{\partial\tau}\right|_{i,j}^{k+1/2} + \phi_{yy|_{i,j}}^{k+1/2} = \phi_{yy|_{i,j}}^{k} - (\nabla\cdot\mathbf{u})_{i,j}^{m} \quad \text{along } j, i = \text{const} \tag{20}$$

$$\left.\frac{\partial\phi}{\partial\tau}\right|_{i,j}^{k+1} + \phi_{xx|_{i,j}}^{k+1} = \phi_{yy|_{i,j}}^{k+1/2} - (\nabla\cdot\mathbf{u})_{i,j}^{m} \quad \text{along } i, j = \text{const} \tag{21}$$

where the superscript k refers to the ADI procedure iteration, m refers to the internal iteration $(m = 1, M)$ within each time step and M the maximum iteration number determined by a condition specifying that $D(\mathbf{u}^M)$ in absolute value is less than a prescribed limit ε. Therefore, the pressure correction ϕ^M is calculated such that

$$D(\mathbf{u}^M) = 0 \tag{22}$$

After convergence of the internal iterative procedure, $\phi^M \to 0$. That way the zero-divergence of velocity is satisfied with the accuracy of the compact finite difference scheme used for velocity and pressure.

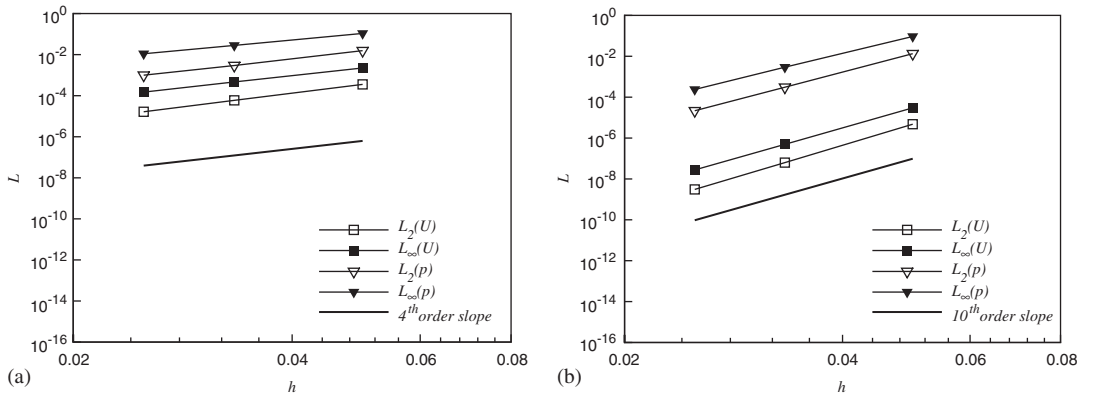

Figure 1. Convergence results for the Taylor vortex solved by fourth- and tenth-order schemes. Results after $\Delta t = 0.02564$ s: (a) fourth-order; and (b) tenth-order.

3. CODE VERIFICATION

The developed algorithm was tested using the Taylor two-dimensional vortex-decay benchmark problem to investigate its accuracy against a known analytical solution

$$U(x, y, t) = -\cos(x)\sin(y)\exp^{-\sigma t} \tag{23}$$

$$V(x, y, t) = \sin(x)\cos(y)\exp^{-\sigma t} \tag{24}$$

$$P(x, y, t) = -\tfrac{1}{4}(\cos(2x) + \cos(2y))\exp^{-2\sigma t} \tag{25}$$

The computational domain considered spans over $0 < x, y < 12\pi$ and $\sigma = 2/Re$, with $Re = 1$ to have convective and diffusive terms with the same order of magnitude. Verification of the method is done via systematic grid convergence testing [18]. Because the exact solutions of the benchmark problems are known, the order of convergence between any two grids, p, can be extracted. Due to the high accuracy of the schemes employed, the solutions were obtained in the domain $0 < x, y < 12\pi$, so that the finer grid error was well above the machine-zero.

In order to quantify the error of each solution, the L_2 and L_∞ error norms are calculated. The convergence of the error norms for the velocity U and pressure p are shown in Figure 1 for the fourth- and tenth-order schemes, respectively. The time chosen corresponds to the time the vortices decay 5% of their original strength. The error norms converge at fourth- and tenth-order rates, verifying the formal accuracy of the schemes employed.

4. INSTABILITY OF TWO-DIMENSIONAL ISOLATED CIRCULAR VORTICES

Kloosterziel and Carnevale [15] have investigated numerically the stability of circular vortices with a radial vorticity given by

$$\overline{\omega}_\alpha(r) = (\tfrac{1}{2}\alpha r^\alpha - 1)\exp(-r^\alpha) \tag{26}$$

The vorticity is negative near the centre and positive further out. The corresponding velocity profiles $\bar{v}_\alpha(r) = -r\exp(-r^\alpha)/2$ increase from zero at $r=0$ to a maximum at $r=(1/\alpha)^{(1/\alpha)}$, falling monotonically to zero. The flow is everywhere clockwise.

For small-enough positive α these vortices are linearly stable. For approximately $\alpha > 1.85$ they become unstable to perturbations with $k=2$. For approximately $\alpha > 3$ they first become unstable to $k=3$ and for $\alpha > 4$ they become unstable to wavenumber-4 instabilities. The growth rates of the most unstable normal modes as a function of for wavenumber $k=2,3$ and 4 were calculated by Kloosterziel and Carnevale [15] and is shown that for large-enough α several azimuthal wavenumbers can simultaneously be unstable.

For a small initial perturbation, unstable modes grow initially in such way as dictated by linear dynamics. However, in order to investigate the non-linear effects for larger amplitudes, the incompressible Navier–Stokes equations need to be solved numerically. In order to onset instabilities, the following initial vorticity perturbation was used:

$$\omega' = \mu\cos(k\theta)\exp\left[\frac{-(\sigma r^\alpha - 2)}{2\sigma^2}\right] \tag{27}$$

where μ and σ are constants and k is an azimuthal wavenumber.

In order to compare our results with other numerical simulations, for each numerical simulation the decomposition in azimuthal components was calculated.

Vorticity fields can be expressed as $\sum_{k=0}^{\infty} w_k$, where

$$\omega_k = f_k(r;t)Re(\mathrm{e}^{\mathrm{i}k\theta+\mathrm{i}\phi_k(r;t)}) \tag{28}$$

$Re(\cdot)$ denotes real part and $\phi_k = 0$ for $k=0$. The $f_k(r;t)$ and the phase factors can numerically be determined using $C_k = f_k\cos(\phi_k)$, $S_k = f_k\sin(\phi_k)$ with

$$\{C_k(r;t), S_k(r;t)\} = \frac{1}{\pi}\int_0^{2\pi} \omega(r,\theta;t)\{\cos(k\theta),\sin(k\theta)\}\,\mathrm{d}\theta \tag{29}$$

This gives a decomposition of the vorticity distribution in azimuthal components. A measure of the amplitude of the azimuthal vorticity for each wavenumber, at a given time, is simply

$$A_k(t) = Q_k^{1/2} = \left(\int_0^{2\pi}\int_0^{\infty} \omega_k^2(r,\theta;t) r\,\mathrm{d}r\,\mathrm{d}\theta\right)^{1/2} \tag{30}$$

where Q_k is the enstrophy associated with wavenumber k. The origin $r=0$ is at the centre of the vortex.

The Navier–Stokes calculations that follow are divided into three sub-sections and are the results for the $k=2,3$ and 4 perturbations. For all calculations the computational domain extends to 10 non-dimensional units for each coordinate direction. This was discretized by a mesh comprising 256×256 nodes. Time was scaled by $|\omega(0)|^{-1}$ and the time-step used was 5×10^{-2}, corresponding to a CFL number of 1.28. The kinematic viscosity was set to $v = 1\times10^{-5}\ \mathrm{m^2\ s^{-1}}$.

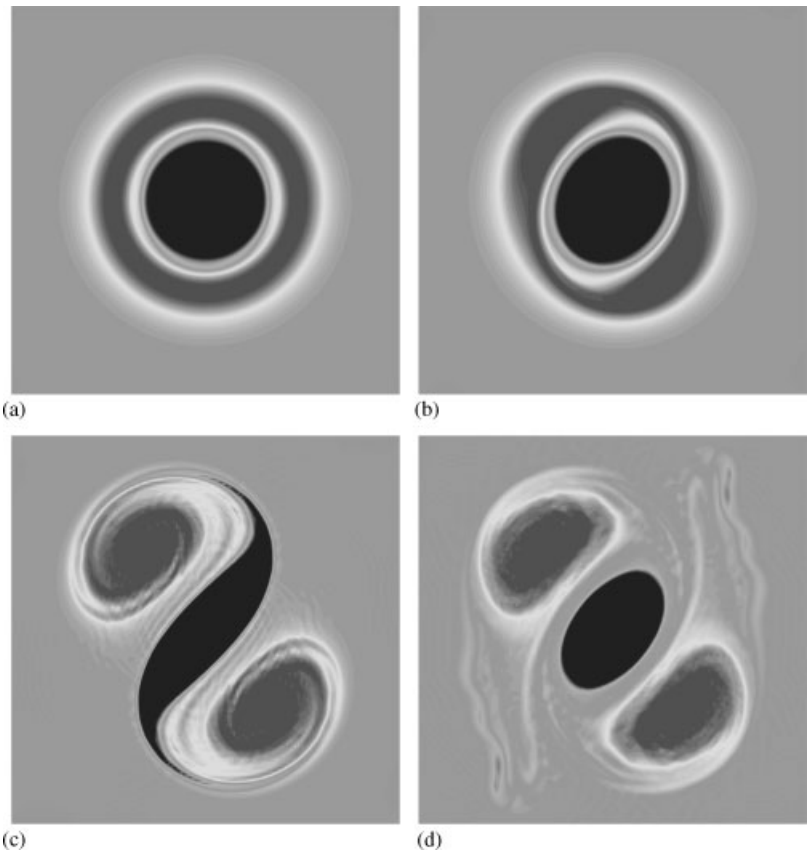

Figure 2. Shaded contour plots of vorticity for a $\overline{\omega}_{\alpha=3}$ vortex initially perturbated with a perturbation of type (27) with $k=2$, $\mu=0.1$, $\sigma=0.25$. Fourth-order results: (a) $t=0$; (b) $t=40$; (c) $t=80$; and (d) $t=200$.

4.1. $k=2$ instability

Figure 2 shows the predicted evolution of the $\alpha=3$ vortex flow with a $k=2$ perturbation given by Equation (27). For this vortex the only unstable normal mode is $k=2$. When this vortex is randomly perturbed, a wavenumber-2 instability emerges. The results correspond to the fourth-order compact scheme.

Figure 2(b) displays the elongated shape of the negative core vorticity, indicating that at $t=40$, A_2 has attained a considerable amplitude. For $t=80$, two satellites, semi-circular areas of positive vorticity, have formed while vorticity filaments start to develop and the core reaches its maximum ellipticity. At $t=120$ (not shown) the core almost returns to a circular shape. From then on the core goes through periodic cycles of elongation. The formed tripole persists afterwards.

Figure 3 shows the evolution of $A_k(t)$ for various even wavenumbers for the simulation shown in Figure 2. Results are shown for both fourth- and tenth-order calculations. Amplitudes

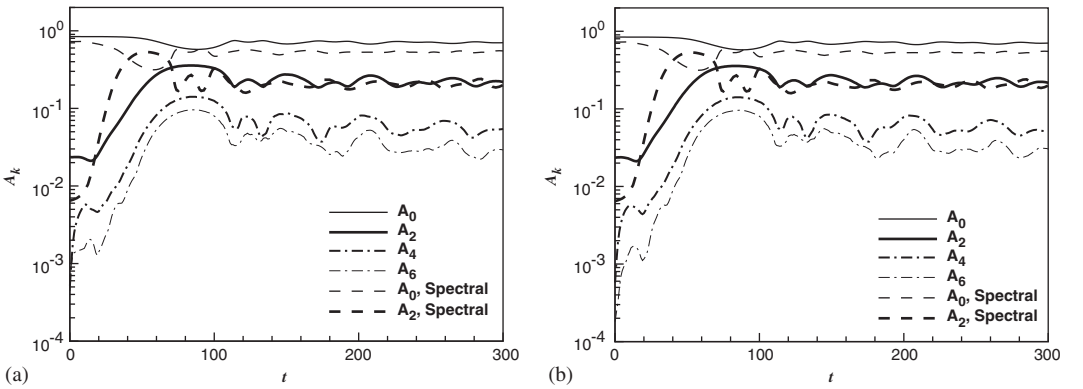

Figure 3. Evolution of amplitudes of various azimuthal components w_k. $k=2$, $\mu=0.1$, $\sigma=0.25$: (a) fourth-order results; and (b) tenth-order results.

for $k>8$ are at all times smaller than A_8. The evolutions of the amplitudes A_k for the fourth- and tenth-order schemes are almost identical, being characterized by an initial transient region, followed by a period of exponential growth of A_2, as predicted by linearized dynamics. Due to non-linear effects, the higher harmonics also grow. For t approximately equal to 80, the amplitudes display a peak. Afterwards, small oscillations appear in all A_k. These oscillations can be traced to the referred cycles of elongation and the return to circularity of the core, which are progressively damped. This rotation is stable and the flow is almost stationary in a co-rotating frame.

In Figure 3 is also shown the evolution for the modal base flow and perturbation wavenumber, A_0 and A_2, respectively, for the spectral results of Reference [15]. Comparing the present results with the spectral results shows that the A_2 peak occurs later for the present results, this difference being attributed to the initial state for $t<20$. The evolution for A_2 is similar for both sets of results. The values for A_2 for $t=300$ are practically the same, indicating that for sufficient large times the amplitude will be the same. This means that the main feature of the flow, defined by the amplitude of the perturbation enstrophy, is well captured.

4.2. $k=3$ *instability*

Figure 4 shows the evolution of a $\alpha=7$ vortex seeded with a $k=3$ perturbation given by Equation (27). This vortex can be unstable to various azimuthal wavenumbers. The initial condition is shown in Figure 4(a). In Figure 4(b) a wavenumber-3 instability is visible, while in Figure 4(c) the core has become triangular and three satellites have formed around the core. In Figure 4(d) the final state is shown. Figure 5 shows the evolution of $A_k(t)$ with $k=2,3,6$ and 9 for the simulation shown in Figure 4. Results are shown for both fourth- and tenth-order results. The peaks of A_3 correspond to a markedly triangular shape of the vortex core. The evolution is similar to that shown in Figure 3 except that A_2 continues to grow even after the triangular vortex has formed, because the $\alpha=7$ vortex calculated is also unstable to $k=2$ perturbations. The differences between both set of results are minimal, making them virtually identical. The results from Reference [15] for A_0 and A_3 are also shown. The agreement of the

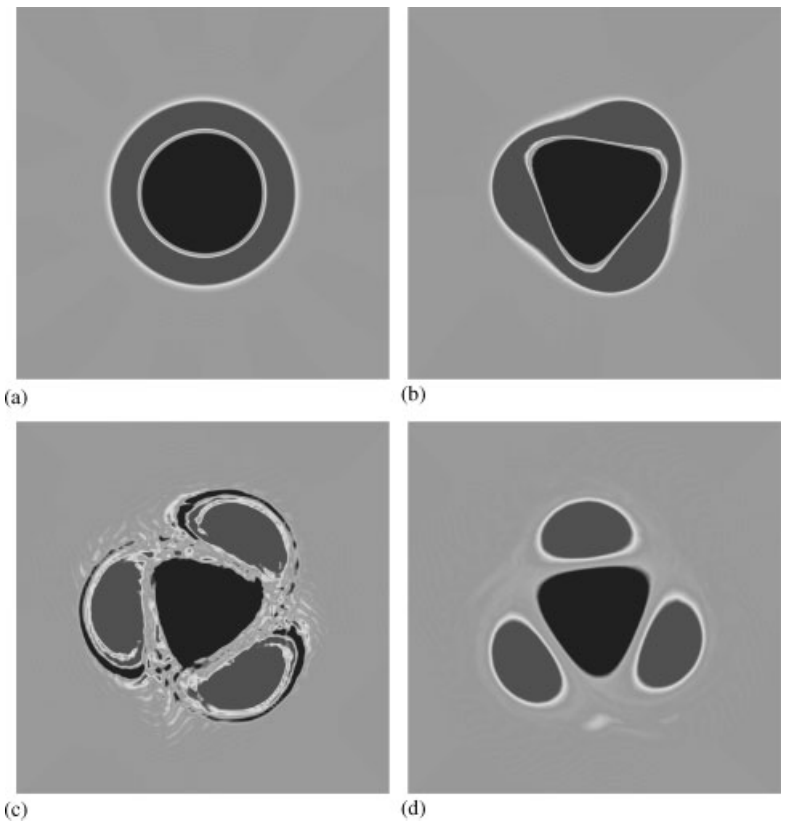

Figure 4. Shaded contour plots of vorticity for a $\overline{\omega}_{\alpha=7}$ vortex initially perturbated with a perturbation of type (27) with $k=3$, $\mu=0.1$, $\sigma=0.5$. Fourth-order results: (a) $t=0$; (b) $t=20$; (c) $t=40$; and (d) $t=200$.

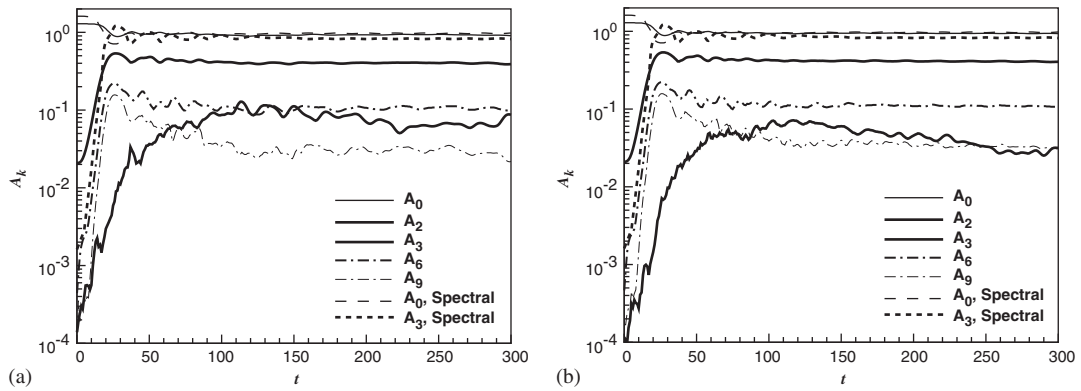

Figure 5. Evolution of amplitudes of various azimuthal components w_k. $k=3$, $\mu=0.1$, $\sigma=0.5$: (a) fourth-order results; and (b) tenth-order results.

present results with the spectral results is good, with the present method capable of closely predicting the time for the occurrence of the peak of A_3.

4.3. $k=4$ *instability*

In Figure 6, we can see the evolution of a $\alpha=7$ vortex seeded with a $k=4$ perturbation of type (27). The initial condition is visually similar to Figure 4(a). In Figure 6(a) the core has become roughly square in shape and four satellites have formed. This square vortex rotates but is unstable to various wavenumber modes. The onset of instability can be seen in Figure 6(b). The satellites move towards each other in pairs and merge. Afterwards the core becomes elongated and breaks up into two vorticity patches. Two dipoles form, which propagate in opposite directions. In Figure 7, the evolution of $A_k(t)$ with $k=0,2,4,8$ and 12 for the simulation shown in Figure 6 can be seen. Results are shown for both fourth- and tenth-order results. After the square vortex formed, A_2 continues to grow and for $t>100$ equals A_4 in amplitude. At this time the core is no longer square and while the $k=2$

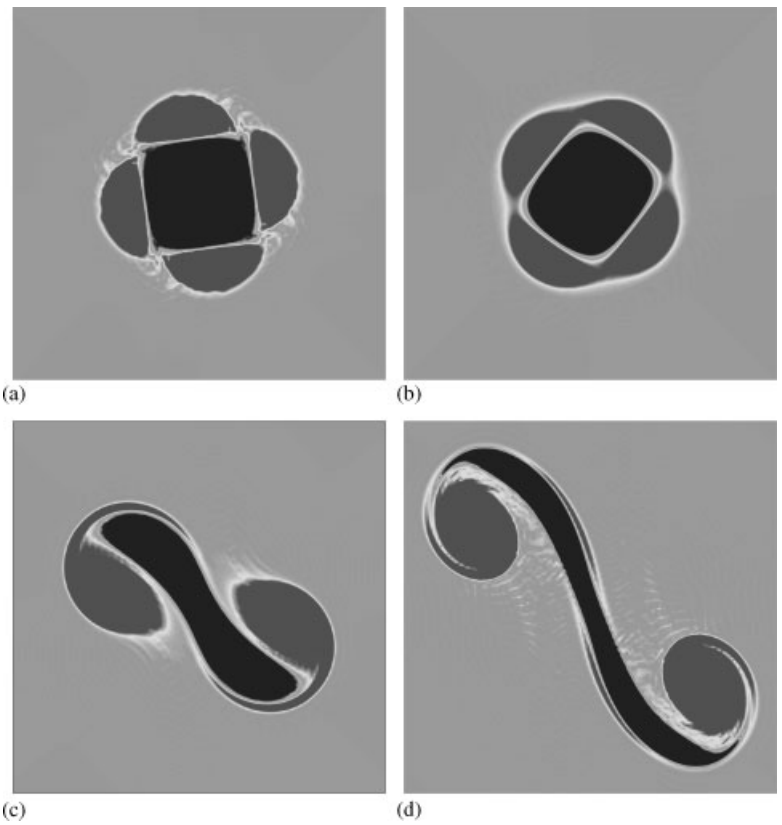

Figure 6. Shaded contour plots of vorticity for a $\overline{\omega}_{\alpha=7}$ vortex initially perturbated with a perturbation of type (27) with $k=4$, $\mu=0.05$, $\sigma=0.5$. Fourth-order results: (a) $t=40$; (b) $t=185$; (c) $t=200$; and (d) $t=210$.

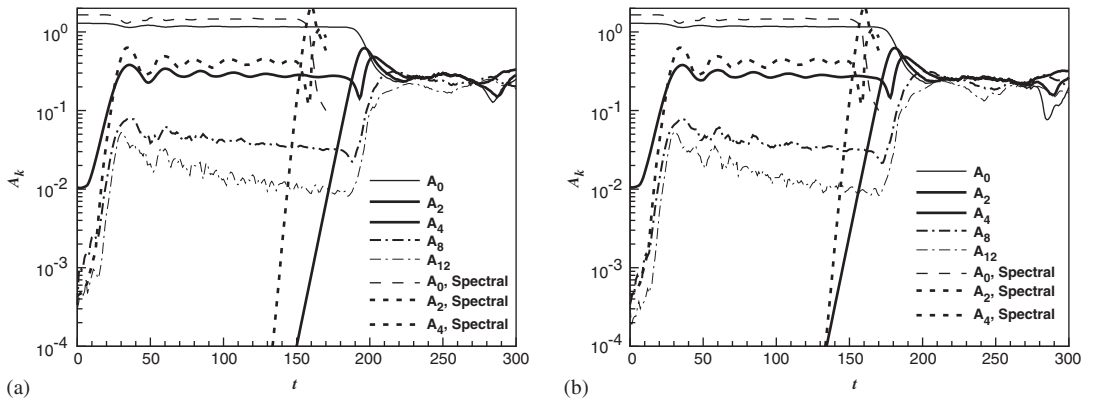

Figure 7. Evolution of amplitudes of various azimuthal components w_k. $k=4$, $\mu=0.05$, $\sigma=0.5$: (a) fourth-order results; and (b) tenth-order results.

component continues to grow, other amplitudes, namely A_4 and A_0 start to dip. These changes are associated with the continued stretching of the core, the merging of the satellites and finally the dipole splitting. In Figure 7, is also shown the evolution for the modal base flow A_0 and perturbation wavenumber A_4, as well as A_2, for the spectral results of Reference [15]. The agreement of the present results with the spectral results is good, with both sets of results capable of predicting the evolutions. The main difference between the fourth- and tenth-order results is on the prediction of the onset of the instability, that is first predicted by the tenth-order scheme. It should be noted that the onset of instability is predicted later for the present results than for the reference results, the tenth-order results being closer. As for the spectral results, the present results show that the break-up of the square vortex is caused by a $k=2$ instability. The growth of A_2 is caused by numerical noise, which indicates that the level of numerical noise is probably higher for the tenth-order scheme.

4.4. Discussion

The formation of a tripole is the most robust phenomenon since it can also arise from randomly perturbed flows. Triangular and square vortices can only be formed when azimuthal perturbations are seeded in the flow. However, all three vortices result of similar evolutions. The perturbation mode growth is followed by the generation of higher harmonics due to non-linear effects. The formation is complete when these non-linear effects halt the growth and amplitudes level off. Amplitudes A_k have the same ordering $A_0 > A_m > A_{2m} > \cdots$, where m is the perturbation wavenumber initially seeded in the flow. The main features of the vortices are captured by the approximation $\omega \approx \omega_0 + \omega_m$. The first harmonic ω_{2m} is of fundamental importance in the formation process, although A_{2m} levels off faster than A_m. Prior to equilibrium, higher harmonics $\omega_{3m}, \omega_{4m}, \ldots$ play a minor role in the formation of the whole structure but are needed to capture the existing small scale filaments. The resolution used, 256^2, resolves these small scale filaments well, even though calculations with 128^2 and 64^2 (not shown) reproduce essentially the same structures, rotating at approximately the same rate.

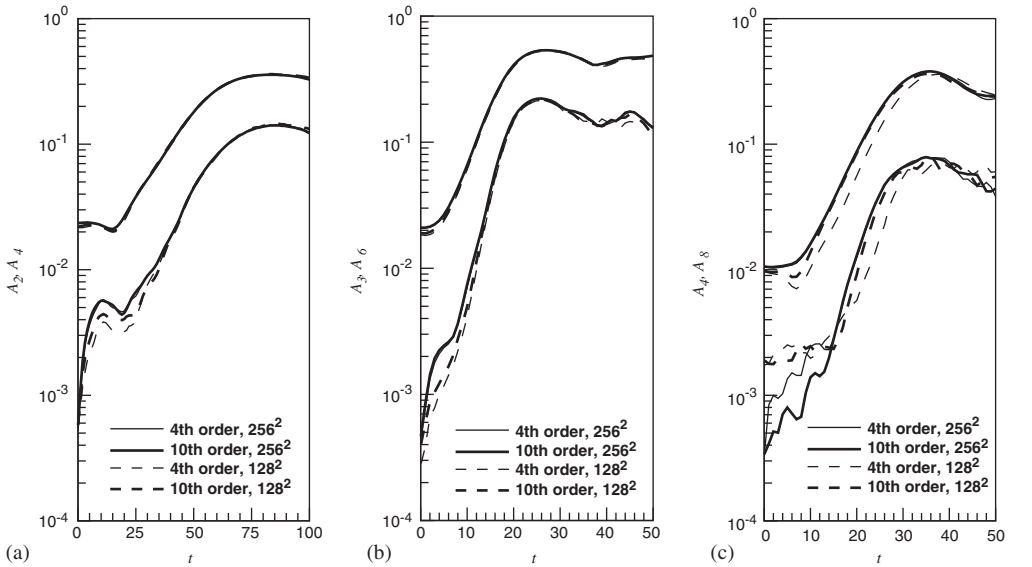

Figure 8. Comparison of amplitudes of the perturbation mode and its first harmonic for two different grid resolutions: (a) $k=2$; (b) $k=3$; and (c) $k=4$.

From the analysis of the evolution of the amplitudes of the azimuthal components ω_k for the three vortices, it is shown that there is no difference in the main features of the flow by using a fourth- or tenth-order spatial discretization for the finer resolution used. The evolution of the amplitudes of ω_0 and ω_m are basically the same for the results with the two compact finite difference operators. Furthermore, the amplitudes of ω_{2m} are very close. The differences are more noticeable for the higher harmonics, namely ω_{3m} and higher, especially as the perturbation mode grows initially.

The differences between the two spatial discretizations used arise when we compare the evolutions of the azimuthal amplitudes A_k for half the reference resolution (Figure 8). During the vortex formation phase, the tenth-order results for ω_m and ω_{2m} are significantly closer to the results for the finer grid than the fourth-order results. This behaviour shows that the highest order spatial discretization is capable of better resolving the main features of the flow for coarser grids, showing a behaviour often mentioned about high-order compact finite differences even though seldom shown: the possibility of obtaining better accuracy for coarser grids.

5. CONCLUSION

Unsteady 2D Navier–Stokes calculations were performed with high-order compact finite difference schemes in which all spatial derivatives were discretized with fourth- or tenth-order accurate compact schemes and fourth-order Runge–Kutta for explicit temporal discretization. The pressure Poisson equation was solved with a false transient ADI method using also compact spatial operators, of the same order of those used in the momentum equations.

The results for the calculations of three azimuthal perturbations to circular vortices are presented. The three different vortex configurations that are obtained result of similar evolutions. The growth of the perturbation mode is accompanied by the generation of higher harmonics due to non-linear effects. The formation is complete when the non-linear effects stop the perturbation mode growth and all amplitudes level off. Comparison of the circular vortex under different modes of perturbation showed that the present method is capable of reproducing the main features of the spectral flow solutions. The calculations display an evolution of the modal enstrophy for the base flow and for the perturbation wavenumber that are in good agreement with the spectral solution for the same resolution.

From the analysis of the evolution of the amplitudes of the azimuthal components ω_k for the three vortices, it is shown that there are negligible differences in the main features of the flow, as defined by the perturbation amplitude and its first harmonic, for both fourth- or tenth-order spatial discretization, when using the reference grid resolution. The differences between the two spatial discretizations used are apparent when we compare the evolutions of the azimuthal amplitudes A_k for half the reference resolution, favouring the tenth-order discretization.

ACKNOWLEDGEMENTS

The authors would like to thank Prof. Grégoire Winckelmans for the initial suggestion to consider the circular vortex benchmark.

REFERENCES

1. Lele SK. Compact finite difference schemes with spectral-like resolution. *Journal of Computational Physics* 1992; **103**:16–42.
2. Schiestel R, Viazzo S. A Hermitian–Fourier numerical method for solving the incompressible Navier–Stokes equations. *Computers and Fluids* 1995; **24**:739–752.
3. Vedy E, Schiestel R, Viazzo S. A high-order finite difference method for incompressible fluid turbulence simulations. *International Journal for Numerical Methods in Fluids* 2003; **42**:1155–1188.
4. Ekaterinaris JA. High-order accurate numerical solutions of incompressible flows with the artificial compressibility method. *International Journal for Numerical Methods in Fluids* 2004; **45**:1187–1207.
5. Brüger A, Gustafsson B, Lötstedt P, Nilsson J. High order accurate solution of the incompressible Navier–Stokes equations. *Technical Report 2003-064*, Uppsala University, Department of Information Technology, 2003.
6. Reuter J, Rempfer D. High order vorticity–velocity method for the simulation of pipe flow transition. *Applied Numerical Mathematics* 2000; **33**:105–111.
7. Cook AW, Dimotakis PE. Transition stages of Rayleigh–Taylor instability between miscible fluids. *Journal of Fluid Mechanics* 2001; **443**:69–99.
8. McWilliams JC. The emergence of isolated coherent vortices in turbulent flow. *Journal of Fluid Mechanics* 1984; **146**:21–43.
9. Legras B, Santangelo P, Benzi R. High-resolution numerical experiments for forced two-dimensional turbulence. *Europhysics Letters* 1988; **5**:37–42.
10. Leith CE. Minimum enstrophy vortices. *Physics of Fluids* 1984; **27**:1388–1395.
11. van Heijst GJF, Kloosterziel RC. Tripolar vortices in a rotating fluid. *Nature* 1989; **338**:569–571.
12. van Heijst GJF, Kloosterziel RC, Williams CWM. Laboratory experiments on the tripolar vortex in a rotating fluid. *Journal of Fluid Mechanics* 1991; **225**:301–331.
13. Carton X, Flierl GR, Polvani L. The generation of tripoles from unstable axisymmetric isolated vortex structures. *Europhysics Letters* 1989; **9**:339–344.
14. Pingree RD, LeCann B. Anticyclonic eddy x91 in the southern bay of Biscay, May 1991 to February 1992. *Journal of Geophysical Research* 1992; **97**:14353–14367.
15. Kloosterziel RC, Carnevale GF. On the evolution and saturation of instabilities of two-dimensional isolated circular vortices. *Journal of Fluid Mechanics* 1999; **388**:217–257.

16. Kloosterziel RC, van Heijst GJF. An experimental study of unstable barotropic vortices in a rotating fluid. *Journal of Fluid Mechanics* 1991; **223**:1–24.
17. Denaro FM. On the application of the Helmholtz–Hodge decomposition in projection methods for incompressible flows with general boundary conditions. *International Journal for Numerical Methods in Fluids* 2003; **43**:43–69.
18. Roache PJ. Verification of codes and calculations. *AIAA Journal* 1998; **36**:696–702.

